Lattice symmetry and emergence of antiferromagnetic quantum Hall states

Morad Ebrahimkhas [1,*], Mohsen Hafez-Torbati [2,3,†] and Walter Hofstetter [2,‡]

[1]*Department of Physics, Mahabad Branch, Islamic Azad University, Mahabad, Iran*
[2]*Institut für Theoretische Physik, Goethe-Universität, 60438 Frankfurt/Main, Germany*
[3]*Lehrstuhl für Theoretische Physik I, Technische Universität Dortmund, Otto-Hahn-Straße 4, 44221 Dortmund, Germany*

Strong local interaction in systems with nontrivial topological bands can stabilize quantum states such as magnetic topological insulators. We investigate the influence of the lattice symmetry on the possible emergence of antiferromagnetic quantum Hall states. We consider the spinful Harper-Hofstadter model extended by a next-nearest-neighbor (NNN) hopping which opens a gap at half filling and allows for the realization of a quantum Hall insulator. The quantum Hall insulator has the Chern number $\mathcal{C} = 2$ as both spin components are in the same quantum Hall state. We add to the system a staggered potential Δ along the $\hat{x}$ direction favoring a normal insulator and the Hubbard interaction U favoring a Mott insulator. The Mott insulator is a Néel antiferromagnet for small NNN hopping and a stripe antiferromagnet for large NNN hopping. We investigate the U-Δ phase diagram of the model for both small and large NNN hoppings. We show that, while for large NNN hopping there exists a $\mathcal{C} = 1$ stripe antiferromagnetic quantum Hall insulator in the phase diagram, there is no equivalent $\mathcal{C} = 1$ Néel antiferromagnetic quantum Hall insulator at the small NNN hopping. We discuss that a $\mathcal{C} = 1$ antiferromagnetic quantum Hall insulator can emerge only if the effect of the spin-flip transformation cannot be compensated by a space-group operation. Our findings can be used as a guideline in future investigations searching for antiferromagnetic quantum Hall states.

I. INTRODUCTION

The role of symmetry in the development of modern condensed matter physics especially in the field of topological insulators (TIs) is unequivocally recognized. Magnetic TIs characterized by a nontrivial topological invariant and long-range magnetic order are promising candidates for application in dissipationless quantum transport, low-energy consumption spintronics, and topological quantum computation [1]. The recent realization of $MnBi_2Te_4$ as the first antiferromagnetic TI has been a key advance in the field of magnetic TIs [2–6].

The experimental achievements in creation of artificial gauge fields [7,8] and in detection of magnetic order [9,10] suggest ultracold atoms trapped in optical lattices [11] as a unique system for simulating magnetic topological quantum states with a high degree of control and tunability of parameters. The Harper-Hofstadter model is realized in optical lattices using laser-assisted tunneling [12,13]. The Haldane model is implemented using the lattice-shaking technique [14]. Further developments are measuring the Chern number of the Hofstadter bands [15] and the Berry curvature of the Bloch bands [16].

Feshbach resonances can be used to tune the interaction between ultracold atoms [17]. The effect of interaction on topological systems has become an interesting problem in recent years [18]. In the spinless Haldane model the nearest-neighbor (NN) interaction induces a transition from a Chern insulator to a charge ordered Mott insulator (MI) [19]. In spinful systems the Hubbard interaction can drive a normal insulator (NI) into a quantum Hall [20–23] or quantum spin Hall insulator [24–27]. Interaction-driven topological transitions are studied also in three-dimensional systems [28,29]. In SU(3) systems, topological transitions from a magnetic insulator into a quantum Hall insulator (QHI) are reported which have no counterparts in the SU(2) case [30].

In the strong-coupling limit the Hubbard interaction favors long-range magnetic order, unless quantum fluctuations are strong enough to stabilize a quantum spin liquid or a valence bond crystal state [31]. This can lead to novel magnetic orders when artificial gauge fields or spin-orbit coupling are present in the system [24,32–34]. In addition, the competition between the band insulator at weak interaction and the Mott insulator at strong interaction can stabilize novel intermediate phases such as antiferromagnetic QHI (AFQHI) with Chern number $\mathcal{C} = 1$ as suggested for the Haldane-Hubbard model [20–22]. In this phase, one of the spin components is in the quantum Hall state and the other is in the normal state.

In this paper we investigate whether the $\mathcal{C} = 1$ AFQHI is a phase specific to the Haldane-Hubbard model or whether it can occur in other interacting topological systems. With this aim we consider the spinful Harper-Hofstadter model in the presence of the Hubbard interaction U, i.e., the Harper-Hofstadter-Hubbard model, at half filling with the plaquette magnetic flux $1/2$ in units of magnetic flux quantum h/e. The flux is the same for both spin components. The

*ebrahimkhas@iau-mahabad.ac.ir
†mohsen.hafez@tu-dortmund.de
‡hofstett@physik.uni-frankfurt.de

155108-1

Harper-Hofstadter model at half filling is gapless and hence we add a next-nearest-neighbor (NNN) hopping to the system to open a gap and realize a QHI [35]. The QHI has the Chern number $\mathcal{C} = 2$. The $\mathcal{C} = 1$ AFQHI in the Haldane-Hubbard model appears as a result of competition between the staggered potential and the Hubbard interaction [20–22]. We include in our model also a staggered potential Δ which favors a NI phase.

II. MODEL AND MAIN RESULTS

The Hamiltonian of the system reads

$$H = H_t + \Delta \sum_{\vec{r},\sigma} (-1)^x n_{\vec{r},\sigma} + U \sum_{\vec{r}} n_{\vec{r},\downarrow} n_{\vec{r},\uparrow} \quad (1)$$

with the hopping term

$$H_t = -\sum_{\vec{r},\sigma} \left(t c_{\vec{r}+\hat{x},\sigma}^\dagger c_{\vec{r},\sigma} + t e^{2\pi i \varphi x} c_{\vec{r}+\hat{y},\sigma}^\dagger c_{\vec{r},\sigma} + t' \right.$$
$$\left. \times e^{2\pi i \varphi (x+1/2)} (c_{\vec{r}+\hat{x}+\hat{y},\sigma}^\dagger c_{\vec{r},\sigma} + c_{\vec{r}+\hat{y},\sigma}^\dagger c_{\vec{r}+\hat{x},\sigma}) + \text{H.c.} \right) \quad (2)$$

where t and t' are the NN and the NNN hoppings, respectively. The fermionic operator $c_{\vec{r},\sigma}^\dagger$ ($c_{\vec{r},\sigma}$) creates (annihilates) a particle at position $\vec{r} = x\hat{x} + y\hat{y} = (x, y)$ with spin component $\sigma = \uparrow, \downarrow$. The position $\vec{r}$ runs over the square lattice and the lattice constant is considered as the unit of length. We define the occupation number operator $n_{\vec{r},\sigma} = c_{\vec{r},\sigma}^\dagger c_{\vec{r},\sigma}$. The parameter φ is the magnetic flux entering each square, in units of the magnetic flux quantum. We fix $\varphi = 1/2$, which is the simplest flux in the Harper-Hofstadter model to achieve topological bands. We would like to point out that other fluxes such as 1/4 can stabilize quantum Hall states with higher Chern numbers [35] and are also interesting to investigate.

The effect of the NNN hopping on the Harper-Hofstadter model is studied in a number of previous works [35–37]. It is included in the Hamiltonian Eq. (1) to open a gap at half filling and realize a QHI [35]. The ratio of the NNN hopping to the NN hopping in optical lattices can be tuned from weak to strong using the lattice shaking technique [38,39].

The second term in Eq. (1) is a staggered potential along the $\hat{x}$ direction, with sublattices A and B acquiring, respectively, the onsite energies $+\Delta$ and $-\Delta$. Such a staggered potential allows a NI to appear in the phase diagram. It can be easily created in optical lattices and is present in the suggested experimental setups [40,41]. Another possibility would be the checkerboard potential which yields an energy offset between the lattice sites with $x + y$ even and the lattice sites with $x + y$ odd. The last term is the Hubbard interaction.

Our proposed model Eq. (1) is the minimal extension of the Harper-Hofstadter-Hubbard model which allows one to examine the existence of a $\mathcal{C} = 1$ AFQHI beyond the Haldane-Hubbard model. One notes that we are considering artificial gauge fields [7,8], which is why no Zeeman term exists in the Hamiltonian Eq. (1).

The Hamiltonian is schematically depicted in Fig. 1(a). For $U = 0$ the Hamiltonian reduces to a two-level problem in momentum space and for finite t' leads to a transition between the QHI and the NI at $\Delta = 2t$ [42]. If there is no flux and no NNN hopping the Hamiltonian recalls the ionic Hubbard
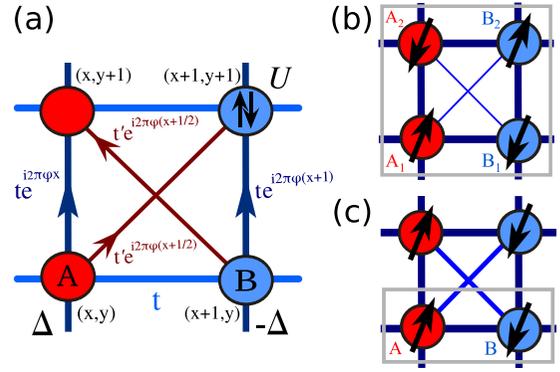
FIG. 1. (a) Schematic representation of the Hamiltonian Eq. (1). Schematic representation of the Néel (b) and the stripe (c) antiferromagnet with the gray box specifying the unit cell.

model with a NI for weak U and a Néel AF for strong U. There are suggestions for intermediate phases [43–49].

We study the phase diagram of the model Eq. (1) in the U-Δ plane both for small and for large NNN hopping, in units of NN hopping t. The results are summarized in Fig. 2. For small NNN hopping there is a transition from the QHI to the Néel antiferromagnet (AF) upon increasing U for $\Delta < 2t$ as can be seen in Fig. 2(a). For $\Delta > 2t$ the QHI separates the NI at weak U from the Néel AF at strong U. For the large NNN hopping in Fig. 2(b) we find that the MI is a stripe AF. An even more interesting difference compared to the small NNN hopping case is the emergence of a $\mathcal{C} = 1$ stripe AFQHI in the limit $U \sim 2\Delta \gg t$. We discuss how the compensation of the spin-flip transformation by a lattice translation prevents a $\mathcal{C} = 1$ Néel AFQHI to appear at small NNN hopping. We present results for the spectral function in the bulk and at the edges. We identify gapless edge states for both spin components in the QHI, and gapless edge states for only one spin component in the $\mathcal{C} = 1$ stripe AFQHI.
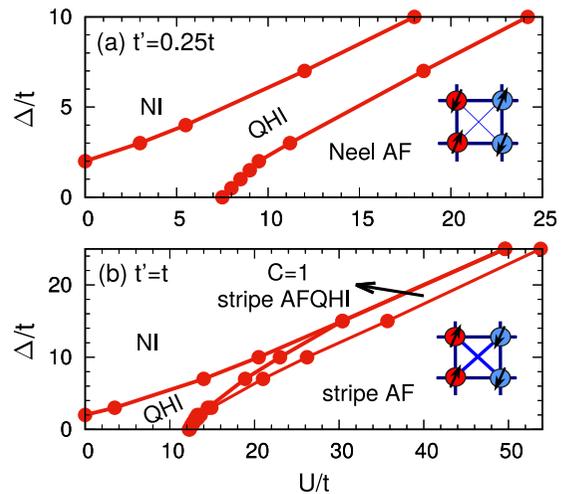
FIG. 2. The phase diagram of the Hamiltonian Eq. (1) for $\varphi = 1/2$ with next-nearest-neighbor hopping $t' = 0.25t$ (a) and $t' = t$ (b). One can identify normal insulator (NI), $\mathcal{C} = 2$ quantum Hall insulator (QHI), Néel and stripe antiferromagnet (AF), and a $\mathcal{C} = 1$ stripe antiferromagnetic QHI (AFQHI) in the phase diagram.

III. METHOD

Dynamical mean-field theory (DMFT) is a highly successful approach to the problem of strongly correlated systems and is exact in the limit of infinite coordination number. For a finite coordination number it is an approximation neglecting the momentum dependence of the self-energy, or the nonlocal quantum fluctuations [50–52]. The $\mathcal{C} = 1$ AFQHI phase predicted by DMFT in the Haldane-Hubbard model [21] is confirmed by exact diagonalization of finite clusters [21] as well as by bold diagrammatic quantum Monte Carlo analysis [22]. A systematic study of nonlocal quantum fluctuations in the Haldane-Hubbard model [23] indicates that a local self-energy can provide an appropriate qualitative description of the topological phase diagram; the momentum dependence of the self-energy is only needed to map out the precise location of the phase boundaries.

We employ the real-space DMFT (RDMFT) approach to qualitatively analyze the phase diagram of the Hamiltonian Eq. (1). The RDMFT was first used to study thin-film geometries [53], and since then has been extended, for example, to address disordered systems [42,54], exotic magnetism [34,55–58], and topological insulators [24,30,59,60]. The local self-energy in the DMFT method [51] becomes position dependent in the real-space extension, allowing for an equal-footing treatment of translationally ordered and disordered systems.

We use the RDMFT implementation introduced in Ref. [61]. We consider 40×40 lattice sizes with periodic boundary conditions (PBC) in both directions unless mentioned otherwise. For selected points close to the phase transitions we have checked that increasing the systems size to 60×60 does not change the results. The temperature is fixed to $T = t/50$, which is much smaller than the energy scales in the system, and we expect to represent the ground-state properties of the model. We use exact diagonalization (ED) as the impurity solver [51,62]. Five bath sites are used for the results that we present unless mentioned otherwise. We have checked that the results for different selected points close to the phase transitions are the same as the results obtained using six and seven bath sites.

The Chern number of the interacting system is determined using the topological Hamiltonian method [63], which relates the Chern number of an interacting system to the Chern number of an effective noninteracting model. The method relies on the adiabatic deformation of the Green's function such that the single-particle gap never closes, leaving the Chern number of the system unchanged. The effective model, called the topological Hamiltonian, in the Bloch form reads

$$\boldsymbol{h}_{\mathrm{top}}(\vec{k}) = \boldsymbol{h}_0(\vec{k}) + \boldsymbol{\Sigma}(\vec{k}, \omega = 0), \qquad (3)$$

where $\boldsymbol{h}_0(\vec{k})$ describes the noninteracting part of the model and $\boldsymbol{\Sigma}(\vec{k}, \omega)$ is the self-energy. In the DMFT the self-energy is local and hence its role in the topological Hamiltonian Eq. (3) is just to modify the onsite energies [64]. One notices that although the topological Hamiltonian method has some limitations and should be used with care [65], it has been applied successfully to similar models [21].
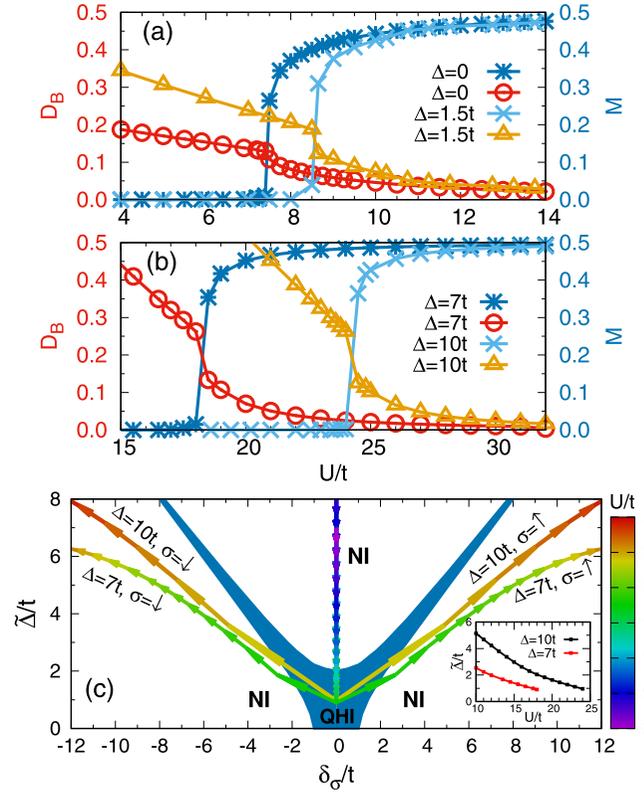
FIG. 3. (a), (b) The local magnetic moment M and the double occupancy D_B on sublattice B plotted vs the Hubbard interaction U for different values of the staggered potential Δ. (c) The evolution of the effective potentials $\tilde{\Delta}$ and δ_σ upon increasing U for $\Delta = 7t$ and $10t$. Here the color indicates the value of U (see the colorbar). The shaded area indicates a quantum Hall insulator (QHI) and the white area indicates a normal insulator (NI). The inset shows $\tilde{\Delta}$ vs U in the paramagnetic region where $\delta_\sigma = 0$. The results are for the next-nearest-neighbor hopping $t' = 0.25t$.

IV. RESULTS

We present results first for the small $t' = 0.25t$ and then for the large $t' = t$ NNN hopping. We avoid the intermediate values $0.6t \lesssim t' \lesssim 0.8t$ where in the large-U limit a quantum spin liquid [66–68] or a valence bond crystal [68–71] is expected, which cannot be captured within our local self-energy approximation. One notices that the Hamiltonian Eq. (1) in the large-U limit is equivalent, up to a weak spatial anisotropy, to the frustrated Heisenberg model with NN and NNN interaction. For $t' = 0.25t$ in Figs. 3(a) and 3(b) we have plotted the local magnetic moment $M_{\vec{r}} = |\langle n_{\vec{r},\uparrow} - n_{\vec{r},\downarrow} \rangle| / 2$ and the double occupancy $D_{\vec{r}} = \langle n_{\vec{r},\uparrow} n_{\vec{r},\downarrow} \rangle$ versus the Hubbard U for different values of the staggered potential Δ. The local moment is position independent, $M_{\vec{r}} =: M$, and we have plotted the double occupancy on sublattice B, shown as D_B. One can identify a transition between a paramagnetic and a magnetic phase, which is shifted to larger values of U as Δ is increased. The paramagnetic phase can be a NI or a QHI, depending on the value of the Chern number $\mathcal{C}$. The magnetic phase is a Néel AF denoted schematically in Fig. 1(b).

There are four sites in the unit cell labeled as A_1, A_2, B_1, and B_2 in Fig. 1(b). The topological Hamiltonian, in the

second quantization form, up to an irrelevant constant can be written as

$$H_{\text{top}} = H_t + \sum_{\vec{r},\sigma} [\tilde{\Delta}(-1)^x + \delta_\sigma(-1)^{x+y}] n_{\vec{r},\sigma} \quad (4)$$

where H_t is the hopping term Eq. (2) and the effective potentials $\tilde{\Delta}$ and δ_σ, in the spirit of Refs. [26,30,72], are given by

$$\tilde{\Delta} = \Delta + \tfrac{1}{4}\big[\Sigma_{A_1}^\sigma(0) + \Sigma_{A_2}^\sigma(0) - \Sigma_{B_1}^\sigma(0) - \Sigma_{B_2}^\sigma(0)\big], \quad (5a)$$

$$\delta_\sigma = \tfrac{1}{4}\big[\Sigma_{A_1}^\sigma(0) - \Sigma_{A_2}^\sigma(0) - \Sigma_{B_1}^\sigma(0) + \Sigma_{B_2}^\sigma(0)\big], \quad (5b)$$

where $\Sigma_X^\sigma(0)$ is the zero-frequency self-energy at the site X with spin σ. $\tilde{\Delta}$ is spin independent and $\delta_\uparrow = -\delta_\downarrow$ (see Appendix A).

The evolution of the effective potentials $\tilde{\Delta}$ and δ_σ upon increasing U for $\Delta = 7t$ and $10t$ is displayed in Fig. 3(c). The shaded area in this figure indicates a QHI and the white area indicates a NI with $\tilde{\Delta}$ and δ_σ treated as independent parameters. Upon increasing U the effective potential $\tilde{\Delta}$ is renormalized [26,30] and the system enters the QHI for $\tilde{\Delta} < 2t$. This is evident from the inset in Fig. 3(c) displaying $\tilde{\Delta}$ versus U in the paramagnetic region where $\delta_\sigma = 0$. Upon entering the magnetic phase the effective potential δ_σ becomes finite and both spin components fall out of the QHI region [73]. This demonstrates that the Néel AF is topologically trivial.

It is apparent from Eq. (4) that the two spin components are always in the same topological state due to $\delta_\uparrow = -\delta_\downarrow$. This makes the emergence of a $\mathcal{C} = 1$ Néel AF impossible. This can also be understood from the symmetry of the phase, without considering the topological Hamiltonian Eq. (4). In the Néel AF illustrated in Fig. 1(b) the effect of the spin-flip transformation can be compensated by a lattice translation, i.e., by a shift by one lattice site along the $\hat{y}$ direction. This suggests that spin-up and spin-down fermion dispersions will differ at most by a shift in momentum space. This is confirmed in Fig. 4(a), which shows an equal spectral function for up and down spin. The spectral function is plotted for $-6t \leqslant \omega \leqslant +6t$. The spectral function in Fig. 4(a) is for $\Delta = 7t$ and $U = 20t$ in the Néel AF and is averaged over the sites in the unit cell. The spectral function at position $\vec{r}$ with spin σ is defined from the local Green's function as $A_{\vec{r},\sigma}(\omega) = (-1/\pi)\text{Im}G_{\vec{r},\sigma}(\omega + i\eta)$ where η is a broadening factor fixed to $0.05t$ in our computations. The single-particle gap equal for up and down spins prevents a $\mathcal{C} = 1$ Néel AF from emerging. The spectral function for $\Delta = 7t$ and $U = 15t$ and different values of x on a 41×40 lattice with open boundary conditions along $\hat{x}$ and PBC along $\hat{y}$ is displayed in Fig. 4(b). The edges are defined at $x = 0$ and 40 and the lattice is symmetric with respect to the center $x = 20$. Six bath sites are used in the impurity problem. There are gapless excitations at the edge which quickly disappear upon approaching the bulk, consistent with the topological Hamiltonian prediction on a QHI phase.

We consider now the large NNN hopping $t' = t$. The MI phase in this case is a stripe AF. The antiferromagnetic ordering is formed along $\hat{x}$ and the ferromagnetic ordering is formed along $\hat{y}$ [see Fig. 1(c)], due to the spatial anisotropy induced by the staggered potential Δ. There are two sites in the unit cell and the topological Hamiltonian for $t' = t$ can be
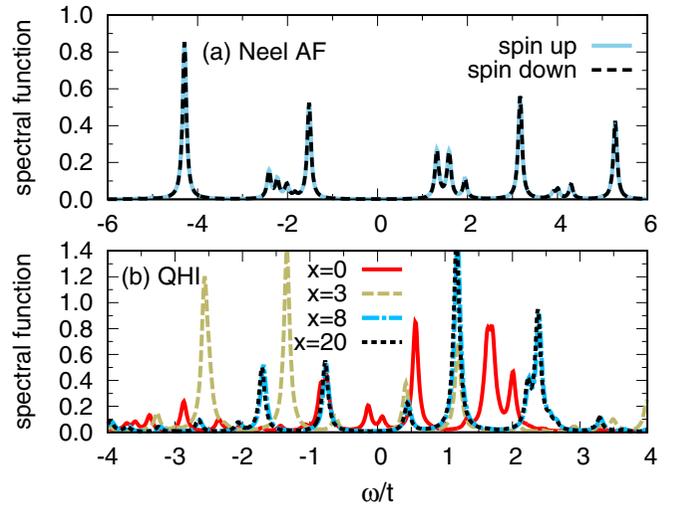
FIG. 4. (a) The bulk spectral function averaged over the sites in the unit cell for up and down spin in the Néel antiferromagnet (AF) with $\Delta = 7t$ and $U = 20t$. (b) The spectral function plotted for different values of x in the quantum Hall insulator (QHI) with $\Delta = 7t$ and $U = 15t$ obtained using a cylindrical geometry with edges at $x = 0$ and 40. The results are for the next-nearest-neighbor hopping $t' = 0.25t$.

expressed, up to an irrelevant constant, as

$$H_{\text{top}} = H_t + \sum_{\vec{r},\sigma} \tilde{\Delta}_\sigma(-1)^x n_{\vec{r},\sigma}, \quad (6)$$

with the effective potential

$$\tilde{\Delta}_\sigma = \Delta + \tfrac{1}{2}[\Sigma_A^\sigma(0) - \Sigma_B^\sigma(0)]. \quad (7)$$

The spin dependence of this effective potential allows different spin components to fall in different topological regions and consequently a $\mathcal{C} = 1$ AFQHI to emerge. The spin component σ is in the quantum Hall state if $|\tilde{\Delta}_\sigma| < 2t$ and in the normal state if $|\tilde{\Delta}_\sigma| > 2t$.

In Figs. 5(a) and 5(b) we have plotted the local magnetic moment M and the effective potential $\tilde{\Delta}_\sigma$ versus U for $\Delta = 10t$ (a) and $15t$ (b). The dashed lines at $\tilde{\Delta}_\sigma = 2t$ and $\tilde{\Delta}_\sigma = -2t$ specify the borders of the topological region $|\tilde{\Delta}_\sigma| < 2t$. A shaded area indicates a phase with a finite Chern number $\mathcal{C}$. One can see from Fig. 5(a) that upon increasing U the effective potential $\tilde{\Delta}_\sigma$ drops below $2t$ at $U \simeq 20t$ and a transition from a NI to a QHI takes place. For $U \gtrsim 23t$ the local magnetic moment becomes finite and $\tilde{\Delta}_\sigma$ becomes spin dependent. One spin component, spin down in the figure, almost immediately leaves the topological region while the other spin component remains topological up to $U \simeq 26t$ [74]. This leads to a $\mathcal{C} = 1$ stripe AFQHI phase for $23t \lesssim U \lesssim 26t$. Beyond $U \simeq 26t$ the system is a (topologically trivial) stripe AF. One can see from Fig. 5(b) that upon increasing Δ to $15t$ the QHI phase disappears and there is only the $\mathcal{C} = 1$ stripe AFQHI between the NI and the stripe AF.

In the stripe AF displayed in Fig. 1(c) the effect of the spin-flip transformation, unlike the Néel AF, cannot be compensated by a lattice translation. This leads to a spin-dependent spectral function (see Appendix B). This allows
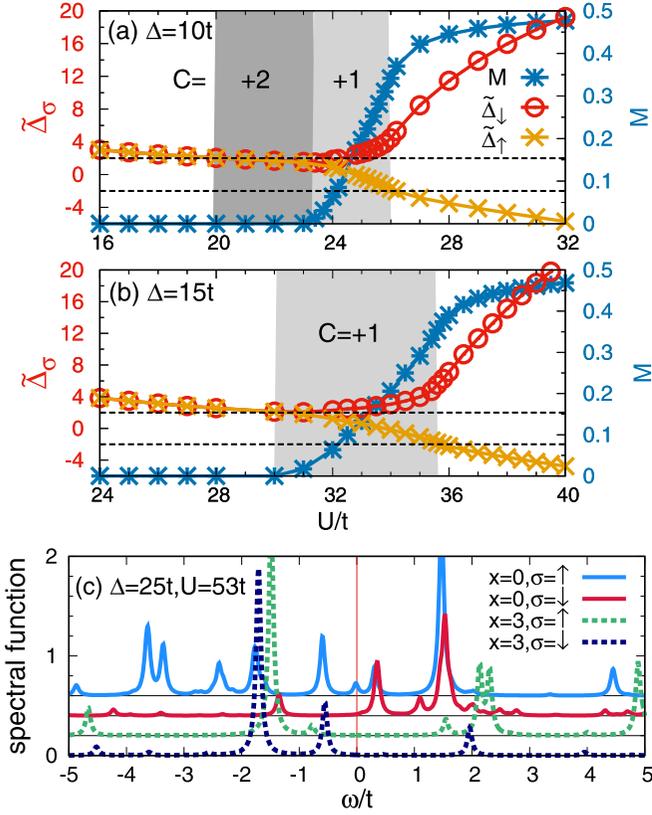
FIG. 5. The local magnetic moment M and the effective potential $\tilde{\Delta}_\sigma$ plotted vs the Hubbard interaction U for $\Delta = 10t$ (a) and $\Delta = 15t$ (b). A shaded area indicates a phase with a finite Chern number $\mathcal{C}$. (c) The edge spectral functions for up and down spin in the $\mathcal{C} = 1$ stripe antiferromagnetic quantum Hall insulator with $\Delta = 25t$ and $U = 53t$, obtained using a cylindrical geometry with edges at $x = 0$ and 40. The shift of the spectral function along the vertical axis is for clarity. The results are for the next-nearest-neighbor hopping $t' = t$.

up- and down-spin components to change their Chern numbers at different transition points and the $\mathcal{C} = 1$ stripe AFQHI to emerge.

In Fig. 5(c) we have plotted the spectral function near the edge $x = 0$ of a 41×40 cylindrical geometry with $\Delta = 25t$ and $U = 53t$, where the system is expected to be a $\mathcal{C} = 1$ stripe AFQHI according to the topological Hamiltonian. The shift of the spectral function along the vertical axis is for clarity. Six bath sites are used in the impurity problem. There are contributions out of the plotted region $-5t \leqslant \omega \leqslant +5t$ which mainly belong to the spin-down spectral function. Edge excitations in an interacting QHI have been discussed using ED on finite clusters [19] and using RDMFT with ED [30] and with the quantum Monte Carlo [24] impurity solver. We are not aware of a study of edge excitations in an interacting $\mathcal{C} = 1$ AFQHI. Although our results in Fig. 5(c) are obtained using a finite number of bath sites and indicate only the qualitative shape of the spectral function, they can still capture the main expected feature that edge excitations are gapless for one spin component and gapped for the other. The edge excitations in optical lattices can be investigated by introducing a Hofstadter interface [59].

V. SUMMARY

To summarize, we compare in Fig. 2 the U-Δ phase diagram of the model Eq. (1) for small $t' = 0.25t$ (a) and large $t' = t$ (b) NNN hopping. Apart from the type of magnetic order, there is a fundamental difference between the two phase diagrams: In Fig. 2(b) there exists an intermediate $\mathcal{C} = 1$ stripe AFQHI while in Fig. 2(a) a $\mathcal{C} = 1$ Néel AFQHI never appears. The absence of the AFQHI in the latter case stems from the fact that the effect of the spin-flip transformation can be compensated by a space-group operation.

We notice that our conclusion on the possible existence of a $\mathcal{C} = 1$ AFQHI is based on the symmetry of the phase and not the details of the model studied in this paper. For example, replacing the staggered potential along $\hat{x}$ in Eq. (1) with the staggered potential $H_\Delta = \sum_{\vec{r},\sigma} \Delta(-1)^{x+y} n_{\vec{r},\sigma}$ changing along both $\hat{x}$ and $\hat{y}$ directions would lead to the opposite situation, i.e., would allow a $\mathcal{C} = 1$ Néel and prevent a $\mathcal{C} = 1$ stripe AFQHI. Our conclusion is consistent with the realization of the $\mathcal{C} = 1$ AFQHI in the Haldane-Hubbard model [20,21]. Our results can be used as a guideline for future experiments, especially in optical lattices, searching for AFQHI phases.

APPENDIX A: TOPOLOGICAL HAMILTONIAN FOR SMALL NEXT-NEAREST-NEIGHBOR HOPPINGS

In this section we derive the topological Hamiltonian Eq. (4), which is valid for small NNN hoppings, i.e., for the case that in the large-U limit the system exhibits a Néel AF. In general, there are four sites in the unit cell as shown in Fig. 1(b). A local self-energy in Eq. (3) leaves the hopping part of the noninteracting Hamiltonian unchanged and modifies only the onsite energies. One finds

$$\varepsilon_{A_1,\sigma} = +\Delta + \Sigma^\sigma_{A_1}(0), \tag{A1a}$$

$$\varepsilon_{A_2,\sigma} = +\Delta + \Sigma^\sigma_{A_2}(0), \tag{A1b}$$

$$\varepsilon_{B_1,\sigma} = -\Delta + \Sigma^\sigma_{B_1}(0), \tag{A1c}$$

$$\varepsilon_{B_2,\sigma} = -\Delta + \Sigma^\sigma_{B_2}(0), \tag{A1d}$$

where $\varepsilon_{X,\sigma}$ represents the onsite energy of the topological Hamiltonian at the position X for the spin component σ. As one can see from Fig. 1(b) the Néel AF is invariant under a spin-flip transformation followed by a one-site lattice translation along $\hat{y}$ direction. This implies the symmetry relation

$$\Sigma^\sigma_{A_1}(\omega) = \Sigma^{\bar{\sigma}}_{A_2}(\omega), \qquad \Sigma^\sigma_{B_1}(\omega) = \Sigma^{\bar{\sigma}}_{B_2}(\omega), \tag{A2a}$$
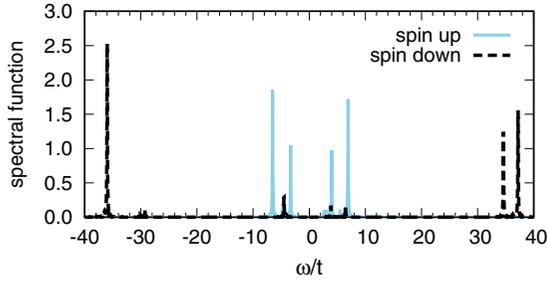
FIG. 6. The spectral function in the stripe antiferromagnetic phase for up and down spins plotted vs the frequency ω. The results are for the staggered potential $\Delta = 15t$, the Hubbard interaction $U = 40t$, and the next-nearest-neighbor hopping $t' = t$.

where $\bar{\sigma}$ indicates the opposite direction of σ. There is the second symmetry relation

$$\Sigma_{A_1}^\sigma(0) - \Sigma_{A_2}^\sigma(0) = \Sigma_{B_2}^\sigma(0) - \Sigma_{B_1}^\sigma(0), \tag{A2b}$$

which we found from our data and is valid only at zero frequency. Equation (A1) can be rewritten as

$$\varepsilon_{A_1,\sigma} = +\Delta + \Sigma_{A_+} + \Sigma_{A_-}^\sigma, \tag{A3a}$$

$$\varepsilon_{A_2,\sigma} = +\Delta + \Sigma_{A_+} - \Sigma_{A_-}^\sigma, \tag{A3b}$$

$$\varepsilon_{B_1,\sigma} = -\Delta + \Sigma_{B_+} + \Sigma_{B_-}^\sigma, \tag{A3c}$$

$$\varepsilon_{B_2,\sigma} = -\Delta + \Sigma_{B_+} - \Sigma_{B_-}^\sigma, \tag{A3d}$$

where we have defined

$$\Sigma_{A_+} := \frac{1}{2}\big[\Sigma_{A_1}^\sigma(0) + \Sigma_{A_2}^\sigma(0)\big], \tag{A4a}$$

$$\Sigma_{A_-}^\sigma := \frac{1}{2}\big[\Sigma_{A_1}^\sigma(0) - \Sigma_{A_2}^\sigma(0)\big], \tag{A4b}$$

and similarly for Σ_{B_+} and $\Sigma_{B_-}^\sigma$. Σ_{A_+} and Σ_{B_+} are independent from σ, and $\Sigma_{A_-}^\sigma = -\Sigma_{A_-}^{\bar{\sigma}}$ and $\Sigma_{B_-}^\sigma = -\Sigma_{B_-}^{\bar{\sigma}}$ due to the symmetry relation Eq. (A2a). The symmetry relation Eq. (A2b) implies $\Sigma_{A_-}^\sigma = -\Sigma_{B_-}^\sigma$. By some straightforward manipulation of Eq. (A3) we get

$$\varepsilon_{A_1,\sigma} = C + \tilde{\Delta} + \delta_\sigma, \tag{A5a}$$

$$\varepsilon_{A_2,\sigma} = C + \tilde{\Delta} - \delta_\sigma, \tag{A5b}$$

$$\varepsilon_{B_1,\sigma} = C - \tilde{\Delta} - \delta_\sigma, \tag{A5c}$$

$$\varepsilon_{B_2,\sigma} = C - \tilde{\Delta} + \delta_\sigma, \tag{A5d}$$

where we have defined the common constant $C := (\Sigma_{A_+} + \Sigma_{B_+})/2$ and the effective potentials

$$\tilde{\Delta} := \Delta + \frac{1}{2}(\Sigma_{A_+} - \Sigma_{B_+}), \tag{A6a}$$

$$\delta_\sigma := \frac{1}{2}(\Sigma_{A_-}^\sigma - \Sigma_{B_-}^\sigma). \tag{A6b}$$

One notices that $\tilde{\Delta}$ is independent from σ and $\delta_\sigma = -\delta_{\bar{\sigma}}$ due to the symmetry relations Eq. (A2). This completes the derivation of Eq. (4) with the effective potentials Eq. (5).

APPENDIX B: SPECTRAL FUNCTION IN THE STRIPE ANTIFERROMAGNETIC PHASE

In Fig. 6 we have plotted the bulk spectral function averaged over the sites in the unit cell in the stripe AF for up and down spins. The results are for the staggered potential $\Delta = 15t$, the Hubbard interaction $U = 40t$, and the next-nearest-neighbor hopping $t' = t$. In contrast to the spectral function in the Néel AF in Fig. 4(a), the spectral function in the stripe AF depends on spin. This is due to the fact that the effect of the spin-flip transformation cannot be compensated by a space-group operation in the stripe AF [see Fig. 1(c)].

[1] Y. Tokura, K. Yasuda, and A. Tsukazaki, Nat. Rev. Phys. **1**, 126 (2019).

[2] D. Zhang, M. Shi, T. Zhu, D. Xing, H. Zhang, and J. Wang, Phys. Rev. Lett. **122**, 206401 (2019).

[3] M. M. Otrokov, I. P. Rusinov, M. Blanco-Rey, M. Hoffmann, A. Y. Vyazovskaya, S. V. Eremeev, A. Ernst, P. M. Echenique, A. Arnau, and E. V. Chulkov, Phys. Rev. Lett. **122**, 107202 (2019).

[4] J. Li, Y. Li, S. Du, Z. Wang, B.-L. Gu, S.-C. Zhang, K. He, W. Duan, and Y. Xu, Sci. Adv. **5**, eaaw5685 (2019).

[5] H. Li, S.-Y. Gao, S.-F. Duan, Y.-F. Xu, K.-J. Zhu, S.-J. Tian, J.-C. Gao, W.-H. Fan, Z.-C. Rao, J.-R. Huang, J.-J. Li, D.-Y. Yan, Z.-T. Liu, W.-L. Liu, Y.-B. Huang, Y.-L. Li, Y. Liu, G.-B. Zhang, P. Zhang, T. Kondo, S. Shin, H.-C. Lei, Y.-G. Shi, W.-T. Zhang, H.-M. Weng, T. Qian, and H. Ding, Phys. Rev. X **9**, 041039 (2019).

[6] M. M. Otrokov, I. I. Klimovskikh, H. Bentmann, D. Estyunin, A. Zeugner, Z. S. Aliev, S. Gaß, A. U. B. Wolter, A. V. Koroleva, A. M. Shikin, M. Blanco-Rey, M. Hoffmann, I. P. Rusinov, A. Y. Vyazovskaya, S. V. Eremeev, Y. M. Koroteev, V. M. Kuznetsov, F. Freyse, J. Sánchez-Barriga, I. R. Amiraslanov, M. B. Babanly, N. T. Mamedov, N. A. Abdullayev, V. N. Zverev, A. Alfonsov, V. Kataev, B. Büchner, E. F. Schwier, S. Kumar, A. Kimura, L. Petaccia, G. Di Santo, R. C. Vidal, S. Schatz, K. Kißner, M. Ìnzelmann, C. H. Min, S. Moser, T. R. F. Peixoto, F. Reinert, A. Ernst, P. M. Echenique, A. Isaeva, and E. V. Chulkov, Nature (London) **576**, 416 (2019).

[7] N. R. Cooper, J. Dalibard, and I. B. Spielman, Rev. Mod. Phys. **91**, 015005 (2019).

[8] M. Aidelsburger, S. Nascimbene, and N. Goldman, C. R. Phys. **19**, 394 (2018).

[9] A. Mazurenko, C. S. Chiu, G. Ji, M. F. Parsons, M. Kanász-Nagy, R. Schmidt, F. Grusdt, E. Demler, D. Greif, and M. Greiner, Nature (London) **545**, 462 (2017).

[10] P. T. Brown, D. Mitra, E. Guardado-Sanchez, P. Schauß, S. S. Kondov, E. Khatami, T. Paiva, N. Trivedi, D. A. Huse, and W. S. Bakr, Science **357**, 1385 (2017).

[11] W. Hofstetter and T. Qin, J. Phys. B **51**, 082001 (2018).

[12] M. Aidelsburger, M. Atala, M. Lohse, J. T. Barreiro, B. Paredes, and I. Bloch, Phys. Rev. Lett. **111**, 185301 (2013).

[13] H. Miyake, G. A. Siviloglou, C. J. Kennedy, W. C. Burton, and W. Ketterle, Phys. Rev. Lett. **111**, 185302 (2013).

[14] G. Jotzu, M. Messer, R. Desbuquois, M. Lebrat, T. Uehlinger, D. Greif, and T. Esslinger, Nature (London) **515**, 237 (2014).

[15] M. Aidelsburger, M. Lohse, C. Schweizer, M. Atala, J. T. Barreiro, S. Nascimbène, N. R. Cooper, I. Bloch, and N. Goldman, Nat. Phys. **11**, 162 (2014).

[16] N. Fläschner, B. S. Rem, M. Tarnowski, D. Vogel, D.-S. Lühmann, K. Sengstock, and C. Weitenberg, Science **352**, 1091 (2016).

[17] I. Bloch, J. Dalibard, and W. Zwerger, Rev. Mod. Phys. **80**, 885 (2008).

[18] S. Rachel, Rep. Prog. Phys. **81**, 116501 (2018).

[19] C. N. Varney, K. Sun, M. Rigol, and V. Galitski, Phys. Rev. B **82**, 115125 (2010).

[20] J. He, Y.-H. Zong, S.-P. Kou, Y. Liang, and S. Feng, Phys. Rev. B **84**, 035127 (2011).

[21] T. I. Vanhala, T. Siro, L. Liang, M. Troyer, A. Harju, and P. Törmä, Phys. Rev. Lett. **116**, 225305 (2016).

[22] I. S. Tupitsyn and N. V. Prokof'ev, Phys. Rev. B **99**, 121113(R) (2019).

[23] T. Mertz, K. Zantout, and R. Valentí, Phys. Rev. B **100**, 125111 (2019).

[24] D. Cocks, P. P. Orth, S. Rachel, M. Buchhold, K. Le Hur, and W. Hofstetter, Phys. Rev. Lett. **109**, 205303 (2012).

[25] J. C. Budich, B. Trauzettel, and G. Sangiovanni, Phys. Rev. B **87**, 235104 (2013).

[26] A. Amaricci, J. C. Budich, M. Capone, B. Trauzettel, and G. Sangiovanni, Phys. Rev. Lett. **114**, 185701 (2015).

[27] K. Jiang, S. Zhou, X. Dai, and Z. Wang, Phys. Rev. Lett. **120**, 157205 (2018).

[28] A. Amaricci, J. C. Budich, M. Capone, B. Trauzettel, and G. Sangiovanni, Phys. Rev. B **93**, 235112 (2016).

[29] B. Irsigler, J.-H. Zheng, F. Grusdt, and W. Hofstetter, Phys. Rev. Research **2**, 013299 (2020).

[30] M. Hafez-Torbati, J.-H. Zheng, B. Irsigler, and W. Hofstetter, Phys. Rev. B **101**, 245159 (2020).

[31] L. Balents, Nature (London) **464**, 199 (2010).

[32] J. Radić, A. Di Ciolo, K. Sun, and V. Galitski, Phys. Rev. Lett. **109**, 085303 (2012).

[33] V. S. Arun, R. Sohal, C. Hickey, and A. Paramekanti, Phys. Rev. B **93**, 115110 (2016).

[34] B. Irsigler, J.-H. Zheng, M. Hafez-Torbati, and W. Hofstetter, Phys. Rev. A **99**, 043628 (2019).

[35] Y. Hatsugai and M. Kohmoto, Phys. Rev. B **42**, 8282 (1990).

[36] J. H. Han, D. J. Thouless, H. Hiramoto, and M. Kohmoto, Phys. Rev. B **50**, 11365 (1994).

[37] D. J. Thouless, Phys. Rev. B **28**, 4272 (1983).

[38] W. Beugeling, J. C. Everts, and C. Morais Smith, Phys. Rev. B **86**, 195129 (2012).

[39] M. Di Liberto, O. Tieleman, V. Branchina, and C. M. Smith, Phys. Rev. A **84**, 013607 (2011).

[40] F. Gerbier and J. Dalibard, New J. Phys. **12**, 033007 (2010).

[41] N. Goldman, I. Satija, P. Nikolic, A. Bermudez, M. A. Martin-Delgado, M. Lewenstein, and I. B. Spielman, Phys. Rev. Lett. **105**, 255302 (2010).

[42] J.-H. Zheng, T. Qin, and W. Hofstetter, Phys. Rev. B **99**, 125138 (2019).

[43] M. Hafez-Torbati and G. S. Uhrig, Phys. Rev. B **93**, 195128 (2016).

[44] S. S. Kancharla and E. Dagotto, Phys. Rev. Lett. **98**, 016402 (2007).

[45] N. Paris, K. Bouadim, F. Hébert, G. G. Batrouni, and R. T. Scalettar, Phys. Rev. Lett. **98**, 046403 (2007).

[46] J. Wang, L. Zhang, R. Ma, Q. Chen, Y. Liang, and T. Ma, Phys. Rev. B **101**, 245161 (2020).

[47] H.-F. Lin, H.-D. Liu, H.-S. Tao, and W.-M. Liu, Sci. Rep. **5**, 9810 (2015).

[48] M. Ebrahimkhas, Phys. Lett. A **375**, 3223 (2011).

[49] A. Shahbazy and M. Ebrahimkhas, Chin. J. Phys. **58**, 273 (2019).

[50] G. Kotliar and D. Vollhardt, Phys. Today **57**, 53 (2004).

[51] A. Georges, G. Kotliar, W. Krauth, and M. J. Rozenberg, Rev. Mod. Phys. **68**, 13 (1996).

[52] W. Metzner and D. Vollhardt, Phys. Rev. Lett. **62**, 324 (1989).

[53] M. Potthoff and W. Nolting, Phys. Rev. B **59**, 2549 (1999).

[54] Y. Song, R. Wortis, and W. A. Atkinson, Phys. Rev. B **77**, 054202 (2008).

[55] M. Snoek, I. Titvinidze, C. Tőke, K. Byczuk, and W. Hofstetter, New J. Phys. **10**, 093008 (2008).

[56] P. P. Orth, D. Cocks, S. Rachel, M. Buchhold, K. L. Hur, and W. Hofstetter, J. Phys. B **46**, 134004 (2013).

[57] M. Hafez-Torbati and W. Hofstetter, Phys. Rev. B **100**, 035133 (2019).

[58] Valli Angelo, Amaricci Adriano, Brosco Valentina, and Capone Massimo, Nano Lett. **18**, 2158 (2018).

[59] B. Irsigler, J.-H. Zheng, and W. Hofstetter, Phys. Rev. Lett. **122**, 010406 (2019).

[60] A. Amaricci, A. Valli, G. Sangiovanni, B. Trauzettel, and M. Capone, Phys. Rev. B **98**, 045133 (2018).

[61] M. Hafez-Torbati and W. Hofstetter, Phys. Rev. B **98**, 245131 (2018).

[62] M. Caffarel and W. Krauth, Phys. Rev. Lett. **72**, 1545 (1994).

[63] Z. Wang and S.-C. Zhang, Phys. Rev. X **2**, 031008 (2012).

[64] We find that the real part of the self-energy at the smallest (in absolute value) Matsubara frequency accurately describes the zero-frequency self-energy obtained by a polynomial fit.

[65] Y.-Y. He, H.-Q. Wu, Z. Y. Meng, and Z.-Y. Lu, Phys. Rev. B **93**, 195164 (2016).

[66] H.-C. Jiang, H. Yao, and L. Balents, Phys. Rev. B **86**, 024424 (2012).

[67] W.-J. Hu, F. Becca, A. Parola, and S. Sorella, Phys. Rev. B **88**, 060402(R) (2013).

[68] D. Poilblanc, M. Mambrini, and S. Capponi, SciPost Phys. **7**, 41 (2019).

[69] R. Haghshenas and D. N. Sheng, Phys. Rev. B **97**, 174408 (2018).

[70] L. Wang, Z.-C. Gu, F. Verstraete, and X.-G. Wen, Phys. Rev. B **94**, 075143 (2016).

[71] L. Capriotti and S. Sorella, Phys. Rev. Lett. **84**, 3173 (2000).

[72] L. Crippa, A. Amaricci, N. Wagner, G. Sangiovanni, J. C. Budich, and M. Capone, Phys. Rev. Res. **2**, 012023(R) (2020).

[73] A continuous evolution of the effective potentials in Fig. 3(c) across the magnetic transition implies an intermediate $\mathcal{C} = 2$ Neel AF to exist. However, this region is so narrow that we could not get any converged RDMFT data within it.

[74] There is a narrow region between the QHI and the $\mathcal{C} = 1$ stripe AFQHI where both spin components are in the topological state. This phase is not specified in the figure as it is very narrow, $\simeq 0.5t$, and may not survive beyond the DMFT approximation.